Changes in Urban Heat Island Effect with the Development of Newtowns

Kyungil Lee
Korea University
Yoonji Kim
Korea University
Hyun Chan Sung
Korea University
Seung Hee Kim
Chapman University
Seong Woo Jeon (eepps_korea@korea.ac.kr)
Korea University

Research Article

Keywords: Newtown , climate and thermal research, urban planning strategies, urban heat islands (UHIs)

Posted Date: April 6th, 2021

DOI: https://doi.org/10.21203/rs.3.rs-382802/v1

Changes in urban heat island effect with the development of Newtowns

Kyungil Lee[1], Yoonji Kim[1], Hyun Chan Sung[1], Seung Hee Kim[2], and Seong Woo Jeon[1]*

[1]Division of Environmental Science & Ecological Engineering, Korea University, 02841 145 Anam-ro, Seongbuk-gu, Seoul, 02841

[2]Center of Excellence in Earth Systems Modeling and Observations, Chapman University, Orange, CA 92866, USA.

*E-mail: eepps_korea@korea.ac.kr

Abstract

Newtown is a planned city built over a short time period. It is suitable for climate and thermal research, particularly formulating urban planning strategies to analyse problems such as urban heat islands (UHIs). Herein, a comprehensive approach was demonstrated for determining changes in UHI distribution during 1989–2048 in two Newtowns with different urban planning. A significant increase in built-up areas was observed from 1989 (< 5%) to 2018 (> 40%) in both Newtowns. However, this increase significantly varied (approximately 12.25%) with urban planning in the areas where UHIs occurred before and after development. Moreover, without effective mitigation, the built-up area in each Newtown is estimated to increase to approximately 60%, and the surface UHI intensity in most areas to increase by 4 °C in 2048. Thus, these results combined with architectural assessment models can improve the understanding of thermal environmental impacts of urbanisation and help mitigate heat island hazards.

Global population growth and urban expansion primarily cause land use and land cover (LULC) changes and increases in built-up area. In 2018, approximately 55.3% of the world's population resided in cities, among which 60% will reside in cities with approximately 0.5 million inhabitants by 2030[1]. Rapidly increasing economic development accelerates these changes, particularly in fast-growing urban areas, hindering sustainable development[2]. LULC changes induced by human activities lead to different local climates than in surrounding areas. This effect, termed as urban heat island (UHI), occurs worldwide[3,4]. UHIs primarily occur due to increased solar radiation absorption and trapping in new surface materials of various infrastructure[5,6]. The magnitude and extent of UHIs are highly positively correlated with urban area and population size in cities; thus, UHIs are significantly affected by urban expansion[7]. UHIs can be divided into two types: meteorological UHI, an increase in local air temperature[8], and surface urban heat island (SUHI), an increase in urban skin temperature[9]. SUHI is particularly evident in spatial variations of upwelling thermal radiance caused by LULC changes and is commonly influenced by the surrounding sub-urban environment[8,9].

Newtown, also called a planned city, is built in a short time period within a pre-determined boundary for specific purposes. Since the mid-to-late twentieth century, Newtowns have been constructed worldwide, contributing to population growth and inflation in large cities[10,11]. Newtowns facilitate climate and thermal research through formulation of urban planning strategies to analyse problems, such as UHIs, and by providing information on the urban temporal temperature variation mechanism[12]. Comparison of UHI changes in Newtowns have not yet been conducted. Carrying out comparative studies on climate effects of urbanisation under different urban planning conditions is particularly difficult because of different urban environments, economic situations, and climates, as well as inconsistent data.

Since 1990, 14 Newtowns have been repopulated or built in sub-urban areas in South Korea to manage population, transportation, and environmental concerns in several large cities. Urban planning in the first-generation Newtowns, providing indiscriminate housing, was not systematic and resulted in negative impacts, such as unplanned urban expansion, environmental degradation, and low greenspace ratio in housing complexes. The second-generation Newtowns were developed through systematic and environmentally friendly urban planning, such as low-density urbanisation and expansion of green areas (Table 1). However, in both cases, an increase in UHI is estimated because of a rapid infrastructural development and vegetation loss. Moreover, the UHI phenomenon may intensify with further urban expansion.

Herein, expansion and intensification of UHI due to Newtown development was empirically analysed using satellite data in two different-generation Newtowns in South Korea (Fig. 1). The SUHI intensity of each Newtown is the difference between the temperatures of built-up and surrounding areas within the boundary[4,13-15]. A Markov chain model, combined with the cellular automata method, determined the SUHI distribution with LULC changes in the two Newtowns. Notably, urban planning influenced the change patterns in the expansion and intensification of UHIs, despite urban expansion. Furthermore, the future SUHI intensities in Newtowns may significantly increase with changes in structural characteristics owing to renovation and additional urban expansion.

Results

LULC changes according to Newtown development. In the accuracy assessment of the three LULC classifications, the kappa coefficient in LULC classification areas for all the three years were greater than 0.8, verifying that these classifications were significant predictors of future LULC and SUHI distribution. LULC analysis showed that the extent and proportion of LULC types varied temporally, and significant transformations were observed between 1989 and 2018. The accumulation of built-up areas in the two Newtowns has been significantly increased during each development period (Fig. 2b and Fig. 3b). However, forest and agricultural areas had significantly declined. In 1989, most of the LULCs in Bundang Newtown and Pangyo Newtown were forest and agricultural areas, accounting for approximately 85% of the total area, while built-up areas accounted for less than 5%. After that, the highest built-up growth occurred in Bundang Newtown between 1989 and 2000, when the development phase of Bundang Newtown was over. The built-up areas increased from 1.47 km^2 (4.39%) to 14.09 km^2 (42.13%); however, agricultural areas significantly decreased from 13.90 km^2 (41.55%) to 2.99 km^2 (8.93%), and forests also considerably decreased from 44.19% to 33.88%. In addition, open spaces increased from 0.46% to 5.68%, which was due to the development of the Newtown, or because it was an area under development at that time (Fig. 2a). In Pangyo Newtown, very little change had occurred because Newtown development planning was not yet established. In the case of built-up areas, the proportion increased from 3.23% to 16.73%, which was confirmed by the construction of the main road within the boundary and unplanned and fragmented development (Fig. 3a). This also evidently increased the percentage of open spaces in this process.

In 2018, when the development of Pangyo Newtown was completed, the proportion of built-up areas in this Newtown considerably increased from 16.73% to 40.81%. Forest areas decreased from 8.17 km^2 (46.38%) to 7.20 km^2 (40.84%) and the remaining agricultural areas decreased to 1.96%, resulting in almost complete urbanisation. In the case of Bundang Newtown, urban expansion occurred through additional urban development and partial renovation between 2000 and 2018. The proportion of built-up areas increased by 7% but agricultural areas decreased by 1.71% (0.57 km^2); indicating almost complete urbanisation. Open spaces that existed in both Newtowns in 2000 were also mostly urbanised in 2018. Due to the low resolution of images, the grass in the built-up areas could not be classified, but the proportion of grass was higher in Pangyo Newtown than in Bundang Newtown as recorded during urban planning. The actual ratio between the two Newtowns would be different. In the case of water bodies, there was no significant change in the areas between 1989 and 2018, but fluctuations due to spectroscopic differences were observed.

SUHI distribution changes according to Newtown development. The accumulation of higher SUHI intensity areas in both the Newtowns had increased with urban expansion (Fig. 2d and Fig. 3d). In 1989, there were no areas in both Bundang and Pangyo Newtowns with a SUHI intensity of six or higher. Most of the areas with evident SUHI phenomenon were agricultural areas and partially urbanised areas. Land surface temperature (LST) is sensitive to vegetation mass, and in Korea, May is an early growing season in agricultural areas that contain less vegetation mass compared to the surrounding forest[16]. This difference in vegetation mass led to a high temperature distribution in agricultural areas in both Newtowns. In 2000, the area with SUHI phenomenon increased by approximately 30% after the development of Bundang Newtown. The areas with SUHI occurrence in the range of 2 °C–4 °C significantly increased from 3.4 km^2 (10.18%) to 10.82 km^2 (32.34%), and those with more than 4 °C, which were few in 1989, increased to approximately 3.03 km^2 (9%) of the total area. In the case of Pangyo Newtown, the areas with the SUHI phenomenon increased by approximately 6.5%, and most of these were distributed across the built main road and surrounding areas. The area with SUHI occurrence in the range 2 °C–4 °C increased from 1.77 km^2 (10.06%) to 3.23 km^2 (18.33%), and those with more than 4 °C were less than 0.324 km^2 (2%) (Fig. 2c). Compared to the developed Bundang Newtown, Pangyo Newtown showed a smaller overall increase in the SUHI phenomenon.

In 2018, when the development of Pangyo Newtown was completed, the areas experiencing the SUHI phenomenon increased by approximately 17%. The areas with SUHI occurrence in the range 2 °C–4 °C increased from 3.23 km^2 (18.33%) to 4.68 km^2 (26.58%), and those in the range 4–6 °C significantly increased from 0.32 km^2 (1.81%) to 2.51 km^2 (14.23%). However, few areas were found that had temperatures greater than 6 °C, and none exceeded 8 °C. For Bundang Newtown, the areas with SUHI < 2 °C had decreased, and the areas with higher SUHI intensity had increased overall. The areas with SUHI in the range 4 °C–6 °C increased from 2.76 km^2 (8.25%) to 3.69 km^2 11.03%, and those with more than 6 °C increased to approximately 2% of the entire Newtown. This implied that the increase in building density and building renovation through additional development may be the main causes of the intensified SUHI phenomenon in existing cities (Fig. 3c).

Buildings are responsible for more than 40% of the global energy consumption, and structural characteristics are related to the UHI intensity[17,18]. Renovation for outdated buildings, such as extension and new construction, intensify the UHI phenomenon[18]. The increase in area and intensity of the SUHI phenomenon before and after Pangyo Newtown development was evidently lower than that of Bundang Newtown. Furthermore, the area with SUHI in the range of 4 °C–6 °C increased higher than that of Bundang Newtown. This may also be due to differences in structural characteristics, such as the average building-to-land ratio, floor area ratio, and height of buildings built in Newtown. The average height and floor area ratio of buildings in the newly constructed housing complex was found to be higher than in Pangyo Newtown, which led to increased UHI intensity.

Predicted LULC for 2028, 2038, and 2048. The cellular automata (CA)-Markov chain model (MCM) analysis predicted that the proportion of built-up areas would increase by approximately 10% from 16.44 km^2 (49.16%) to 19.78 km^2 (59.12%) between 2018 and 2048 in Bundang Newtown (Fig 2a). Moreover, it predicted decreases in forest areas from 35.61% to 29.9% and the grass cover from 12.76% to 10.69%. As Newtown development in the past primarily occurred through transformation of agricultural areas to built-up areas, it was not predicted that a significant urban expansion would occur through deforestation. In addition, most of the buildings in the housing complex of Bundang Newtown were completed in 1990, over 25 years ago. Therefore, renovations are planned for most of these old apartment complexes to improve the poor residential environment and meet the latest urban housing requirements. Hence, most urban expansion was predicted to occur through renovation within the existing built-up areas and partial transformation of the forest surrounding the Newtown.

In the case of Pangyo Newtown, the proportion of urban expansion between 2018 and 2048 was predicted to be higher than that of Bundang Newtown. According to the CA-MCM prediction, built-up areas would increase by approximately 18.42% from 40.81% to 59.23%, the forest areas would decrease from 40.84% to 32.25%, and the grass cover including golf courses would decrease from 15.34% to 7.92% (Fig. 3a). The primary trend observed in the predicted urban expansion was that non-urban areas, such as forest and grass, surrounding the main road were transformed into built-up areas. In contrast with Bundang Newtown, Pangyo Newtown is public-transportation-oriented. During the past Newtown development, the areas surrounding the main road that existed outside the city were underdeveloped. However, if urban expansion occurs in the future, it would be evident primarily in areas with good road proximity. In addition, urban expansion due to the completion of development in the open spaces that were under development in 2018, and further development within the city was also predicted. In terms of agricultural area and water, both Newtowns were predicted to remain almost unchanged from 2018, with little fluctuation.

Predicted SUHI distribution for 2028, 2038, and 2048. CA-MCM predicted the increase in area and intensity of the SUHI phenomenon in both Newtown and, unlike LULC prediction, a significant change was predicted. In Bundang Newtown, the areas where the SUHI phenomenon occurs would increase by approximately 5% between 2018 and 2048. For SUHI intensity distribution, the areas with SUHI ≤ 4 °C would decrease from 17.12 km^2 (51.16%) to 11.44 km^2 (34.21%). Simultaneously, the areas with SUHI > 4 °C was estimated to increase from 4.25 km^2 (12.73%) to 10.68 km^2 (34.71%), affecting the lower SUHI intensity areas. It is predicted that SUHI intensity would expand and increase from the existing residential area, which may reflect the renovation trend partially occurring between 2000 and 2018. Therefore, development of sustainable renovation guidelines is required such as thermal insulation, replacement of the insulation material, and improving the air tightness of the building envelope through renovation using insulation materials[19]. In addition, the areas with SUHI > 6 °C are predicted to increase from 0. 56 km^2 (1.7%) to 2.77 km^2 (8.28%). It has been observed that the higher the LST, the higher the frequency of heat waves at regional scales[20]. In the future, additional thermal environmental policies and energy policies are required for areas where SUHI intensity is expected to increase significantly (Fig. 3a).

In the case of Pangyo Newtown, the areas where the SUHI phenomenon occurred were predicted to increase by 20%. The affected areas are similar to those predicted to change from forests existing around the main road to built-up areas. For SUHI intensity distribution, the area with SUHI ≤ 4 °C would decrease from 7.75 km^2 (43.97%) to 5.08 km^2 (28.83%). Moreover, the areas with SUHI > 4 °C would increase from 2.53 km^2 (14.34%) to 8.7 km^2 (49.36%), and most areas were in the range 2 °C–4 °C (49%) (Fig. 3c). Therefore, it can be predicted that urban features, such as structural characteristics, materials, and building disposition type would change according to the housing complex newly built through Newtown development.

Discussion

This study is the first attempt to simulate and compare the pattern of UHI occurrence according to Newtown development using remote sensing and GIS technology. This discussion focuses on the principal two contributions of the proposed research in comparison with previous studies. Afterwards, the limitations are discussed.

The main contribution of our study is that the different patterns of changes in land use land cover and SUHI phenomenon depending on urban planning were visually and quantitatively shown for the study sites excluding external influences. To provide some examples, Tran et al.[7] and Clinton&Gong[8] do comparative analysis of SUHI phenomenon between cities under different environment or urban situation. Tran et al.[7] examine the spatial patterns of SUHIs for Asian mega cities based on the season and relationship with surface properties. Clinton&Gong[8] estimate the magnitude of SUHI for urban areas between latitudes 71 and – 55 for the year 2010 using MODIS datasets. The results of these studies were successful in demonstrating the contribution of urbanization to the SUHI effect as well as investigating the differences in SUHI between urban and surrounding areas. However, applying these methods could not provide insight into the effect of different urban development types or urban planning on UHI phenomenon. In addition, in terms of comparing the UHI phenomenon between cities, there were some limitations which may lower the reliability of comparison. They all used satellite images constructed at different times and the magnitude of SUHI depends on weather a single image or composite over a period of time is used[14]. In comparison with these previous studies, this research provides a significant contribution by quantifying the influence of the urban planning involved in the UHI phenomenon based on a scientific approach in condition which external influences are controlled. The developed LULC maps showed significant changes in LULC before and after the development of Newtown from 1989 to 2018. The primary driver for the development of both the Newtowns was the transformation of agricultural areas to built-up areas. Moreover, the increase in built-up areas evidently intensified the SUHI phenomenon of an entire Newtown. However, the areas where the SUHI phenomenon additionally occurred or the SUHI intensity increased, were different according to the urban plan. These differences indicated the requirement and importance of urban planning to maintain a sustainable thermal environment, even with rapid LULC changes.

Our research also improves on the predictive models previously developed to study and predict usually LULC patterns. Unlike previous studies, Cellular Automata Markov Chain model was used for prediction of LULC changes and SUHI distribution changes accordingly in study areas. In the case of existing studies, the LULC change was simply predicted using the same model, but there was a limitation in not examining the urban climate change or other possible effects[24,45-47]. Sha et al.[22] and Traiq&Shu[57] tried to examine the LST change according to the LULC change. However, it did not predict the change of the LST distribution according to the predicted future LULC, and as in previous studies, indirect prediction was performed by simply constructing a regression equation using the spectral index. In addition, the LST value may vary depending on the radiative and aerodynamic properties of the satellite image and it is difficult to confirm the relative temperature increase in the built-up areas according to urban growth using LST distribution[14]. In this study, the predicted results based on variations between 2000 and 2018 also showed a possible future pattern of further urban expansion and similar changes in SUHI distribution and intensity in both Newtowns. In addition, through prediction analysis, the importance of building renovation and structural characteristics in urban-level thermal environment changes was also suggested. When renovating old buildings in the future, sustainable renovation methods such as increasing the insulation of facades with new surfaces are required to minimise changes in the thermal environment.

While the presented study provides useful method and information regarding the current and future status of the UHI phenomenon, it is still faced some limitations. This study does not consider additional parameters typically influencing the urban growth because of the specificity of the study area. As mentioned, Newtown is the planned city where the physical and legal aspects of the site were reviewed through feasibility analysis beforehand, the complication associated with urban expansion is relatively low for Newtown. However, the factors for urbanisation are related to the complexity of the terrain, degree of socio-economic development, urban regulations, etc[24]. Therefore, it is necessary to consider additional factors for urban expansion when applying this methodology to a region other than Newtown in the future. In addition, a model that explains the detailed behaviour of UHI using a combination of building renovation and structural characteristics is still necessary. Future research studies should attempt to obtain structural and temporal data over the same period of time and develop models able to explain the change of UHI based on structural characteristics changed by building renovation.

Conclusions

Although the research methods and measures face certain conceptual and practical challenges, this study suggested a proximate causal relationship between urban expansion and SUHI phenomenon change according to urban planning. It is easy to apply for practitioners and the necessary data for application are available without complex acquisition procedures or unopened access datasets. Therefore, the proposed novel method may be applied to both existing and newly-built cities to predict future UHI distribution according to urban planning. Furthermore, the findings and methods constructed through this research can be useful to policy makers, urban planners, researchers, and citizens to adopt sustainable thermal environment management practices including adaptation and mitigation strategies for the city.

Methods

Data acquisitions and pre-processing. Three Landsat images from May with an image quality of nine and cloud cover less than 2% were used to minimise the seasonal influence and cloud cover of each period: 1989, 2000, and 2018. Two Landsat 5 thematic mapper (TM) and one Landsat 8 operational land imager/thermal infrared sensor (OLI/TIRS) images were obtained from the United States Geological Survey - Center for Earth Resources Observation and Science (USGS-EROS) (http://earthexplorer.usgs.gov/). The images were used for LULC classification and SUHI calculation, and each period showed the change trends before and after the Newtown development. The remotely sensed data is an indirect measurement considering the intervening atmosphere and the surface radiative properties that influence the emission and reflection of radiation within the spectral wavelengths detected by the sensor[9]. Atmospheric correction using the dark object subtraction (DOS) method and radiometric correction for pre-processing using the semi-automatic classification (SCP) plugin in QGIS 3.14, were applied to the images. Atmospheric scattering and absorption caused the imaging system to record a non-zero digital number (DN) value for dark objects. The DOS method subtracted the constant non-zero DN value, DN haze, from the whole band, assuming that some objects under complete shadow must have zero reflectance[21].

Land use land cover classification. A supervised classification technique was used with the maximum likelihood classifier (MLC) algorithm to generate LULC maps for each year using the SCP plugin in QGIS 3.14. The MLC-based supervised classification approach was comprehensively used and considered as an established technique in many previous studies for urban LULC classification, where the spatial heterogeneity of pixels is similarly high[22-24]. The MLC algorithm is based on probability density distribution functions (likelihood), includes all training inputs for each land cover class, and has been proven to be an accurate and robust algorithm because it does not overestimate the class values during the computational process[23-25]. In addition, there are some advantages of the MLC algorithm, such as (1) auto-allocation of pixels to the unclassified regions based on the surrounding values[25], and (2) the variance and covariance values of the class signatures are considered within the class distribution[26]. The Landsat images of 1989, 2000, and 2018 were classified into six major LULC classes, (i) built-up areas, covering the buildings and concrete areas; (ii) forest, covering coniferous and broadleaf forests; (iii) grass, covering natural and artificial grass; (iv) open spaces, covering natural and artificial bare areas; (v) agricultural areas, covering paddy field, dry field, etc.; and (vi) water bodies, covering ponds, lakes, and wetlands.

Assessment of classification accuracy is necessary to ensure that classification data can detect changes; this was conducted on the resulting classified imagery through an error matrix and kappa index that enables differentiation between ground-truth and predicted classification[24,27]. High-resolution Google Earth data and aerial photographs provided by the National Geographic Information Institute (NGII) of South Korea were used to establish ground-truth regions for the evaluation of classification accuracy (http://map.ngii.go.kr/). High-resolution data from Google Earth have been used as reference in many classification studies and national standardised land cover maps; NGII provides high-resolution aerial photographs captured since 1945, and can also be used for accuracy assessment[22,24,28]. The kappa coefficient was calculated using equation (1):

$$kappa - coefficient = \frac{n\sum_{i=1}^{k} n\,ii - \sum_{i=1}^{k}(G_i C_i)}{n^2 - \sum_{i=1}^{k}(G_i C_i)} \tag{1}$$

where *i* is the class number; n is the total number of points; n_{ii} is the number of pixels belonging to the actual data class *i*, which were classified as class *i*; C_i is the total number of classified pixels belonging to class *i*; and G_i is the total number of actual data belonging to class *i*. Fifty sample points per class for each Newtown, except water class, were selected automatically by QGIS 3.14. A minimum of 50 samples must be collected for each land cover class in the error matrix to avoid the risk of a biased sample during accuracy assessment[29].

LST estimation. LST estimation using ArcMap 10.5 includes transforming DNs to radiance (L_λ), measuring radiance brightness temperatures (T_B), and adjusting emissivity to extract surface temperature from brightness maps[30]. The LST values were obtained using thermal bands from Landsat TM (B6) and Landsat OLI/TIRS (B10) because of the USGS recommendation to avoid using TIRS band 11 because of its higher calibration uncertainty.

Every object on the Earth emits thermal electromagnetic radiation when its temperature is above absolute zero (K), and the signal received by the thermal sensors can be transformed to radiance (L_λ) using equation (2):

$$L_\lambda = M_L \times Q_{CAL} + A_L \tag{2}$$

where L_λ is the spectral radiance in W/($m^{2\times}$sr×μm); M_L is the radiance multiplicative scaling factor for the band; A_L is the radiance additive scaling factor for the band; and Q_{cal} is the level 1 pixel value in DN, whose values are obtained from the metadata of the Landsat images. After the DN value was converted to radiance, the radiance values were converted to T_B using equation (3):

$$T_B = K_2/\ln[(K_1/L_\lambda) + 1] - 273.15 \tag{3}$$

where T_B is the At-satellite brightness temperature and K_1 and K_2 represent the band-specific thermal conversion constants from the metadata. To obtain the temperature in Celsius, the radiant temperature is revised[30]. The final step in estimating the LST is to rectify the TB using land surface emissivity (LSE, ε) correction as shown in equation (4)[31]:

$$LST = \frac{T_B}{\lfloor 1 + \lfloor \frac{\lambda \times T_B}{\rho} \rfloor \times \ln \epsilon \rfloor} \tag{4}$$

where λ is the wavelength of the emitted radiance (= 10.895 μm); ρ = h × c/σ (1.438×10^{-2} m K), where h is Planck's constant (6.626 × 10–34 Js), c is the velocity of light (2.998 × 108 m/s), and σ is the Boltzmann constant (1.38 × 10–23 J/K); and ε is the emissivity[30,32].

The obtained values of T_B were referenced as a black body, whose properties are different from that of real objects on the Earth's surface and would also be different from real LST[33]. The LST values across a city can have a wide range, and it depends on LULC states constructed within the city. Furthermore, LSE, which is essential for estimating the LST, has strong land use/land cover dependence[34,35].

The LSE value is calculated conditionally using equation (5), and the condition is represented by the formula for each emissivity value[36,37]:

$$\epsilon_{\lambda} = \epsilon_{\lambda v} P_v + \epsilon_{\lambda s}(1 - P_v) + C_{\lambda} \tag{5}$$

where ε_v and ε_s are the vegetation and soil emissivity, respectively and C_λ is the surface roughness (C = 0 for homogeneous and flat surfaces), with a constant value of 0.005[38]. When the normal difference vegetation index (NDVI) is less than $NDVI_S = 0.2$, it is classified as bare soil and its emissivity value is acquired from the reflectance values in the red region (ρR)[39]. The NDVI values between 0.2 and 0.5 are considered as mixtures of soil and vegetation surfaces, and equation (5) is used for extracting their emissivity values. In the equation, $\varepsilon_{\lambda v}$ is the emissivity value of vegetation (= 0.9863 μm) and $\varepsilon_{\lambda s}$ is emissivity value of soil (= 0.9668 μm) in this range[40]. When the NDVI value is larger than $NDVI_v = 0.5$, it is considered as a vegetation surface and an emissivity value of 0.99 is assigned to it[30]. Visible red and near-infrared (NIR) bands were used for calculating NDVI using equation (6). In addition, NDVI values were used to evaluate the proportion of the vegetation (P_v) related to emissivity (ε) using equation (7)[41,42]. A method for calculating P_v using the NDVI values for vegetation soil, which can be applied in global conditions, was suggested in a previous study[36].

$$NDVI = \frac{NIR - RED}{NIR + RED} \tag{6}$$

$$P_V = \lfloor \frac{NDVI - NDVI_S}{NDVI_V - NDVI_S} \rfloor^2 \tag{7}$$

Urban expansion prediction. An integrated CA method combined with MCM was used for predicting urban expansion in 2028, 2038, and 2048 under the business-as-usual scenario of both Newtowns. The CA-MCM is a hybrid and robust algorithm in spatial and temporal dynamic modelling of LULC changes that includes the deterministic modelling framework, spatially explicit approach with stochastically based temporal framework[43,44]. In addition, CA-MCM analysis allows the user to add factors related to urban expansion into the model to improve accuracy, and it can be a support tool for land use planners and policy makers to establish future land use policies[45]. Furthermore, MCM is a tool used to evaluate adjustments in land use among cycles by a sequence of values that depend on the present state[46]. MCM defines the present temporal LULC change to predict future change, and equation (8) presents the calculation of land use change prediction[47]:

$$S(t, t+1) = Pij \times S(t) \tag{8}$$

where S(t) is the system state at time t, S (t+1) is the system state at time t+1, and P_{ij} is the transition probability matrix in a state, which is calculated using equation (9).

$$P_{ij} = \begin{vmatrix} P_{1,1} & P_{1,2} & \cdots & P_{1,N} \\ P_{2,1} & P_{2,2} & \cdots & P_{2,N} \\ \cdots & \cdots & \cdots & \cdots \\ P_{N,1} & P_{N,2} & \cdots & P_{N,N} \end{vmatrix} \quad (0 \le P_{ij} \le 1) \tag{9}$$

P is the Markov probability matrix, P_{ij} is the probability of converting from current state *i* to another state j in prediction time, and P_N is the state probability of any time. Low transition pixels have a low probability value near (0), and high-transition pixels have a high probability value near (1)[47]. The 2000 LULC map of the study area was used as the first base (t_1), and the 2018 LULC map was used as the other (t_2) to obtain the transition probability matrix in this study. However, MCM cannot completely predict the LULC change because it does not consider spatial knowledge distribution within each category, and transition probabilities are not constant among LULC states; therefore, it may suggest the appropriate degree of change but not the appropriate direction[48].

CA is a dynamic process model used for land use cover change[45]. CA has the ability to change its state according to the principle that each cell with its own characteristics can represent parcels of land and self-growth interactions as they are dynamic and can duplicate[49]. Land use changes for any location (cells) can be defined by the existing state and changes in the neighbouring cells, and the growth of objects is simulated in two directions[45]. Hence, CA-MCM, which incorporates the theories of Markov chain analysis and CA, has the advantages of forecasting in terms of utilising time series and space, and can achieve improved simulation for temporal and spatial patterns of land use changes[50]. Multi-criteria evaluation (MCE) was used to determine the LULC classes suitable for changing from the original state to another. MCE combines the factors driving urban growth and fuzzy systems analysis to construct transition suitability maps that show the probability that a pixel would change to another land cover class or remain unchanged[51]. The determinants and spatial expansion of urbanisation are related to the complexity of the terrain, degree of socio-economic development, urban regulations, etc[24]. However, in the case of Newtowns, as the physical and legal aspects of the site were reviewed through feasibility analysis, the complexity associated with urban expansion is relatively low.

In contrast, during urban planning in Newtowns, physical planning and transportation infrastructure are more important for large-scale development to generate housing sites within a short period. Transportation infrastructure, in particular, stimulates and guides urban growth by improving accessibility[52-54]. In addition, slope is an uncontrollable environmental factor that affects urban growth, because construction of buildings and development of cities on steep-slope terrain is difficult or sometimes impossible[55]. Hence, the distance to the main road, slope, and distance to the existing urban area were used to calculate transition suitability maps in this study. The maps of the road and digital elevation model (DEM) were obtained from National Spatial Data in Infrastructure Portal (NSDIP) (http://data.nsdi.go.kr/). Fuzzy membership functions were used to standardise suitability maps into 0–1, where 0 represents unsuitable locations and 1 represents ideal locations for urbanisation. The area of each land class to be transformed into another LULC class was estimated based on the transition probabilities. These areas were separated by the number of iterations performed for CA to predict the areas to be converted per iteration. The future assignment of each cell to an LULC class was based on the suitability of the cell for that LULC class and the similarity of the cell with neighbouring cells of the same class. A contiguity filter of 5×5 pixels was used to define the effect of neighbouring pixels on the central pixel.

Mapping and prediction of the SUHI distribution. The UHI effect occurs due to the anthropogenic modification of natural landscapes in the city boundary layer, and as the urban area increases, the UHI intensity also increases[14]. In addition, LST and SUHI effects are particularly related to the surrounding sub-urban environment[8,14]. To analyse this trend, the SUHI intensity of each Newtown was defined as the difference between the temperatures of an urban area and its surrounding areas (LULC, excluding built-up area) within the boundary[4,13,15]. Thus, the SUHI intensity distribution maps for each Newtown and each period were constructed using two steps. (1) The SUHI intensity variation was calculated using equation (10):

$$\text{SUHI intensity distribution} = T_s - (T_{mean} + 0.5 \times \delta)_{\text{surrounding area}} \quad (10)$$

where T_s is the LST (°C) distribution of Newtown, and T_{mean} and δ are the mean and standard deviation of LST in non-urban areas of Newtown. By subtracting the average temperature of non-urban areas from the temperature of the entire city, it may be verified that the actual SUHI effect was due to urban expansion, rather than the temporary LST value. In addition, the water bodies were excluded while calculating the SUHI intensity because it can irregularly influence the surface temperature (Lee et al, 2020). (2) The SUHI intensity variation was classified into six appropriate ranges: (i) value ≤ 0 °C, (ii) 0 °C < value ≤ 2 °C, (iii) 2 °C < value ≤ 4 °C, (iv) 4 °C < value ≤ 6 °C, (v) 6 °C < value ≤ 8 °C, (vi) 8 °C < value. Thus, the difference in distribution and intensity of the SUHI phenomenon can be compared according to the change in LULC for each Newtown at each time period. In addition, classes are divided into value ranges, to facilitate future SUHI intensity distribution prediction using CA-Markov analysis. The indices, which were positively and negatively correlated with LST, were used to develop transition suitability maps for predicting the SUHI distribution. The normalised difference built-up index (NDBI) was used as the index that highly correlated with LST[56]. NDBI is the most widely accepted tool for the identification of built-up areas and has shown a high surface temperature correlation in previous studies[13,22,57]. The NDBI value was calculated using equation (11):

$$NDBI = \frac{SWIR - NIR}{SWIR + NIR} \quad (11)$$

Built-up areas are sensitive under the 1.55–1.75 wavelength range in the short-wave infrared (SWIR) band; however, they are less sensitive under the 0.79–0.90 wavelength range in the NIR band[58]. The NDBI values range from -1 to +1, and values near +1 generally represent highly dense built-up areas. Furthermore, NDVI was used as the index that weakly correlated with LST. NDVI is the most common index for vegetation extraction and has shown a strong negative correlation with LST in previous studies[32,57,59]. Fuzzy membership functions were also used to standardise the factor maps to 0–1, where 0 represents a low SUHI potential and 1 represents a high SUHI potential.

Data availability

Satellite images from 1989 to 2018 used in this study are freely available at httl://earthexplorer.usgs.gov/. Other datasets are available upon request from K. Lee (leedake@korea.ac.kr).

References

1. United Nations. The World's cities in 2018. *Department of Economic and Social Affairs, Population Division, World Urbanization Prospects* 1–34 (2018).
2. Liping, C., Yujun, S., & Saeed, S. Monitoring and predicting land use and land cover changes using remote sensing and GIS techniques—A case study of a hilly area, Jiangle, China. *PloS One* **13(7),** e0200493 (2018).
3. Eliasson, I. The use of climate knowledge in urban planning. *Landsc. Urban Plan.* **48(1–2),** 31–44 (2000).
4. Lee, K., Kim, Y., Sung, H. C., Ryu, J., & Jeon, S. W. Trend analysis of urban heat island intensity according to urban area change in Asian mega cities. *Sustain.* **12(1),** 112 (2020).
5. Grimmond, S. U. Urbanization and global environmental change: local effects of urban warming. *Geogr. J.* **173(1),** 83–88 (2007).
6. Santamouris, M. Using cool pavements as a mitigation strategy to fight urban heat island—A review of the actual developments. *Renew. Sustain. Energy Rev.* **26,** 224–240 (2013).
7. Tran, H., Uchihama, D., Ochi, S., & Yasuoka, Y. Assessment with satellite data of the urban heat island effects in Asian mega cities. *Int. J. Appl. Earth Obs. Geoinform.* **8(1),** 34–48 (2006).
8. Clinton, N., & Gong, P. MODIS detected surface urban heat islands and sinks: Global locations and controls. *Remote Sens. Environ.* **134,** 294–304 (2013).
9. Voogt, J. A., & Oke, T. R. Thermal remote sensing of urban climates. *Remote Sens. Environ.* **86(3),** 370–384 (2003).
10. Khammar, G. Analysis the Environmental Impacts of Pardis New Town By TOPSIS Model. *Int. J. Manag. Sci. Bus. Res.* **2(7),** 134-141 (2013).
11. Wakeman, R.. *Practicing Utopia: An Intellectual History of the New Town Movement* Ch. 2 (University of Chicago Press, 2016).
12. Qaid, A., Lamit, H. B., Ossen, D. R., & Shahminan, R. N. R. Urban heat island and thermal comfort conditions at micro-climate scale in a tropical planned city. *Energy Build.* **133,** 577–595 (2016).
13. Guha, S., Govil, H., Dey, A., & Gill, N. Analytical study of land surface temperature with NDVI and NDBI using Landsat 8 OLI and TIRS data in Florence and Naples city, Italy. *Eur. J. Remote Sens.* **51(1),** 667–678 (2018).
14. Oke, T., *et al*. *Urban Climates* Ch. 7 (Cambridge University Press, 2017)
15. Zhou, B., Rybski, D., & Kropp, J. P. On the statistics of urban heat island intensity. *Geophys. Res. Lett.* **40(20),** 5486–5491 (2013).
16. Raymond, W. H., Rabin, R. M., & Wade, G. S. Evidence of an agricultural heat island in the lower Mississippi River floodplain. *Bull. Am. Meteorol. Soc.* **75(6),** 1019–1026 (1994).
17. Huovila, P. *Buildings and Climate Change: Status, Challenges, and Opportunities* Ch. 1 (UNEP/Earthprint. 2007

).

18. Li, Y., Schubert, S., Kropp, J. P., & Rybski, D. On the influence of density and morphology on the Urban Heat Island intensity. *Nature Commun.* **11(1),** 1–9 (2020).

19. Häkkinen, T., *et al. Methods and Concepts for Sustainable Renovation of Building* Ch. 4 (VTT Technical Research Centre of Finland: Espoo, Finland, 2012).

20. Yeh, S. W., *et al.* The record-breaking heat wave in 2016 over South Korea and its physical mechanism. *Mon. Weather Rev*. **146(5),** 1463–1474 (2018).

21. Nazeer, M., Nichol, J. E., & Yung, Y. K. Evaluation of atmospheric correction models and Landsat surface reflectance product in an urban coastal environment. *Int. J. Remote Sens.* **35(16),** 6271–6291 (2014).

22. Saha, P., Bandopadhyay, S., Kumar, C., & Mitra, C. Multi-approach synergic investigation between land surface temperature and land-use land-cover. *J. Earth Syst. Sci*. **129(1),** 1–21 (2020).

23. Sun, J., Yang, J., Zhang, C., Yun, W., & Qu, J. Automatic remotely sensed image classification in a grid environment based on the maximum likelihood method. *Math. Computer Model*. **58(3–4),** 573–581 (2013).

24. Wang, S. W., Munkhnasan, L., & Lee, W. K. Land use and land cover change detection and prediction in Bhutan's high altitude city of Thimphu, using cellular automata and Markov chain. *Environmental Challenges.* **2,** 100017 (2020).

25. Al-Ahmadi, F. S., & Hames, A. S. Comparison of four classification methods to extract land use and land cover from raw satellite images for some remote arid areas, Kingdom of Saudi Arabia. *Earth* **20(1),** 167–191 (2009).

26. Erbek, F. S., Özkan, C., & Taberner, M. Comparison of maximum likelihood classification method with supervised artificial neural network algorithms for land use activities. *Int. J. Remote Sens*. **25(9),** 1733–1748 (2004).

27. Yuan, D. A simulation comparison of three marginal area estimators for image classification. *Photogramm. Eng. Remote Sens*. **63(4),** 385–391 (1997).

28. Lee, K., *et al.* The Integration of Remote Sensing and Field Surveys to Detect Ecologically Damaged Areas for Restoration in South Korea. *Remote Sens*. **12(22),** 3687 (2020).

29. Congalton, R. G. A review of assessing the accuracy of classifications of remotely sensed data. *Remote Sens. Environ.* **37(1),** 35–46 (1991).

30. Avdan, U., & Jovanovska, G. Algorithm for automated mapping of land surface temperature using LANDSAT 8 satellite data. *J. Sens.* **2016,** 1-8 (2016).

31. Artis, D. A., & Carnahan, W. H. Survey of emissivity variability in thermography of urban areas. *Remote Sens. Environ*. **12(4),** 313–329 (1982).

32. Weng, Q., Lu, D., & Schubring, J. Estimation of land surface temperature–vegetation abundance relationship for urban heat island studies. *Remote Sens. Environ*. **89(4),** 467–483 (2004).

33. Shen, H., Huang, L., Zhang, L., Wu, P., & Zeng, C. Long-term and fine-scale satellite monitoring of the urban heat island effect by the fusion of multi-temporal and multi-sensor remote sensed data: A 26-year case study of the city of Wuhan in China. *Remote Sens. Environ*. **172,** 109–125 (2016).
34. Mallick, J., Singh, C. K., Shashtri, S., Rahman, A., & Mukherjee, S. Land surface emissivity retrieval based on moisture index from LANDSAT TM satellite data over heterogeneous surfaces of Delhi city. *Int. J. Appl. Earth Obs. Geoinform*. **19,** 348–358 (2012).
35. Radhi, H., Fikry, F., & Sharples, S. Impacts of urbanisation on the thermal behaviour of new built up environments: A scoping study of the urban heat island in Bahrain. *Landsc. Urban Plan*. **113,** 47–61 (2013).
36. Sobrino, J. A., Jiménez-Muñoz, J. C., & Paolini, L. Land surface temperature retrieval from LANDSAT TM 5. *Remote Sens. Environ.* **90(4),** 434–440 (2004).
37. Wang, F., *et al.* An improved mono-window algorithm for land surface temperature retrieval from Landsat 8 thermal infrared sensor data. *Remote Sens.* **7(4),** 4268–4289 (2015).
38. Sobrino, J. A., & Raissouni, N. Toward remote sensing methods for land cover dynamic monitoring: Application to Morocco. *Int. J. Remote Sens.* **21(2),** 353–366 (2000).
39. Sekertekin, A., & Bonafoni, S. Land surface temperature retrieval from Landsat 5, 7, and 8 over rural areas: assessment of different retrieval algorithms and emissivity models and toolbox implementation. *Remote Sens*. **12(2),** 294 (2020).
40. Yu, X., Guo, X., & Wu, Z. Land surface temperature retrieval from Landsat 8 TIRS—Comparison between radiative transfer equation-based method, split window algorithm and single channel method. *Remote Sens.* **6(10),** 9829–9852 (2014).
41. Carlson, T. N., & Ripley, D. A. On the relation between NDVI, fractional vegetation cover, and leaf area index. *Remote Sens. Environ*. **62(3),** 241–252 (1997).
42. Tucker, C. J. Red and photographic infrared linear combinations for monitoring vegetation. *Remote Sens. Environ*. **8(2),** 127–150 (1979).
43. Kamusoko, C., Aniya, M., Adi, B., & Manjoro, M. Rural sustainability under threat in Zimbabwe–simulation of future land use/cover changes in the Bindura district based on the Markov-cellular automata model. *Appl. Geogr*. **29(3),** 435–447 (2009).
44. Keshtkar, H., & Voigt, W. A spatiotemporal analysis of landscape change using an integrated Markov chain and cellular automata models. *Model. Earth Syst. Environ*. **2(1),** 10 (2016).
45. Hamad, R., Balzter, H., & Kolo, K. Predicting land use/land cover changes using a CA-Markov model under two different scenarios. *Sustain*. **10(10),** 3421 (2018).
46. Aaviksoo, K. Simulating vegetation dynamics and land use in a mire landscape using a Markov model. *Landsc. Urban Plan*. **31(1-3),** 129–142 (1995).

47. Kumar, S., Radhakrishnan, N., & Mathew, S. Land use change modelling using a Markov model and remote sensing. *Geomat. Nat. Hazards Risk* **5(2),** 145–156 (2014).

48. Boerner, R. E., *et al.* Markov models of inertia and dynamism on two contiguous Ohio landscapes. *Geogr. Anal.* **28(1),** 56–66 (1996).

49. Brown, D. G., Walker, R., Manson, S., & Seto, K. Modeling land use and land cover change. In *Land change science* (pp. 395–409). (Springer, Dordrecht, 2012).

50. Sang, L., Zhang, C., Yang, J., Zhu, D., & Yun, W. Simulation of land use spatial pattern of towns and villages based on CA–Markov model. *Math. Computer Model*. **54(3–4),** 938–943 (2011).

51. Myint, S. W., & Wang, L. Multicriteria decision approach for land use land cover change using Markov chain analysis and a cellular automata approach. *Can. J. Remote Sens*. **32(6),** 390–404 (2006).

52. Anas, A., Arnott, R., & Small, K. A. Urban spatial structure. *J. Econ. Lit.* **36(3),** 1426–1464 (1998).

53. Hu, Z., & Lo, C. P. Modeling urban growth in Atlanta using logistic regression. *Computers Environ. Urban Syst.* **31(6),** 667–688 (2007).

54. Kasraian, D., Maat, K., & van Wee, B. The impact of urban proximity, transport accessibility and policy on urban growth: A longitudinal analysis over five decades. *Environ. Plan. B* **46(6),** 1000–1017 (2019).

55. Kechebour, B. E. Relation between stability of slope and the urban density: case study. *Proced. Eng*. **114,** 824–831 (2015).

56. Zha, Y., Gao, J., & Ni, S. Use of normalized difference built-up index in automatically mapping urban areas from TM imagery. *Int. J. Remote Sens.* **24(3),** 583–594 (2003).

57. Tariq, A., & Shu, H. CA-Markov Chain Analysis of Seasonal Land Surface Temperature and Land Use Land Cover Change Using Optical Multi-Temporal Satellite Data of Faisalabad, Pakistan. *Remote Sens*. **12(20),** 3402 (2020).

58. Bhatti, S. S., & Tripathi, N. K. Built-up area extraction using Landsat 8 OLI imagery. *GIScience Remote Sens.* **51(4),** 445–467 (2014).

59. Sun, H., Chen, Y., & Zhan, W. Comparing surface-and canopy-layer urban heat islands over Beijing using MODIS data. *Int. J. Remote Sens*. **36(21),** 5448–5465 (2015).

Figures with legends

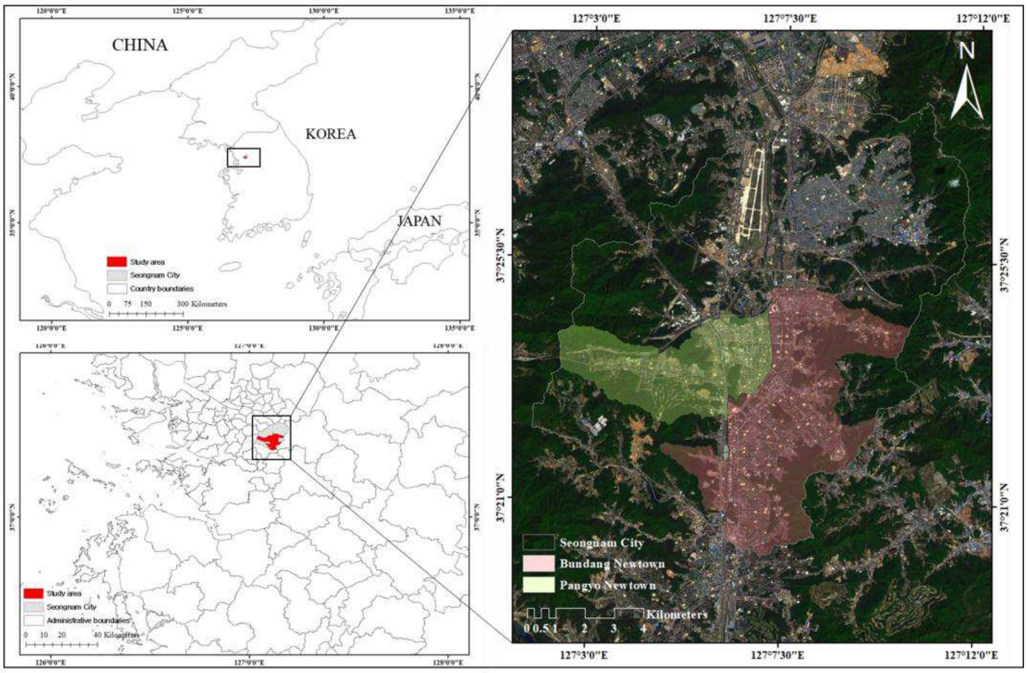

Fig. 1 Map of study area. a. Geographical location of the two Newtowns. **b.** Enlarged image showing the Newtowns. **c.** Landsat OLI image acquired on May 09, 2018.

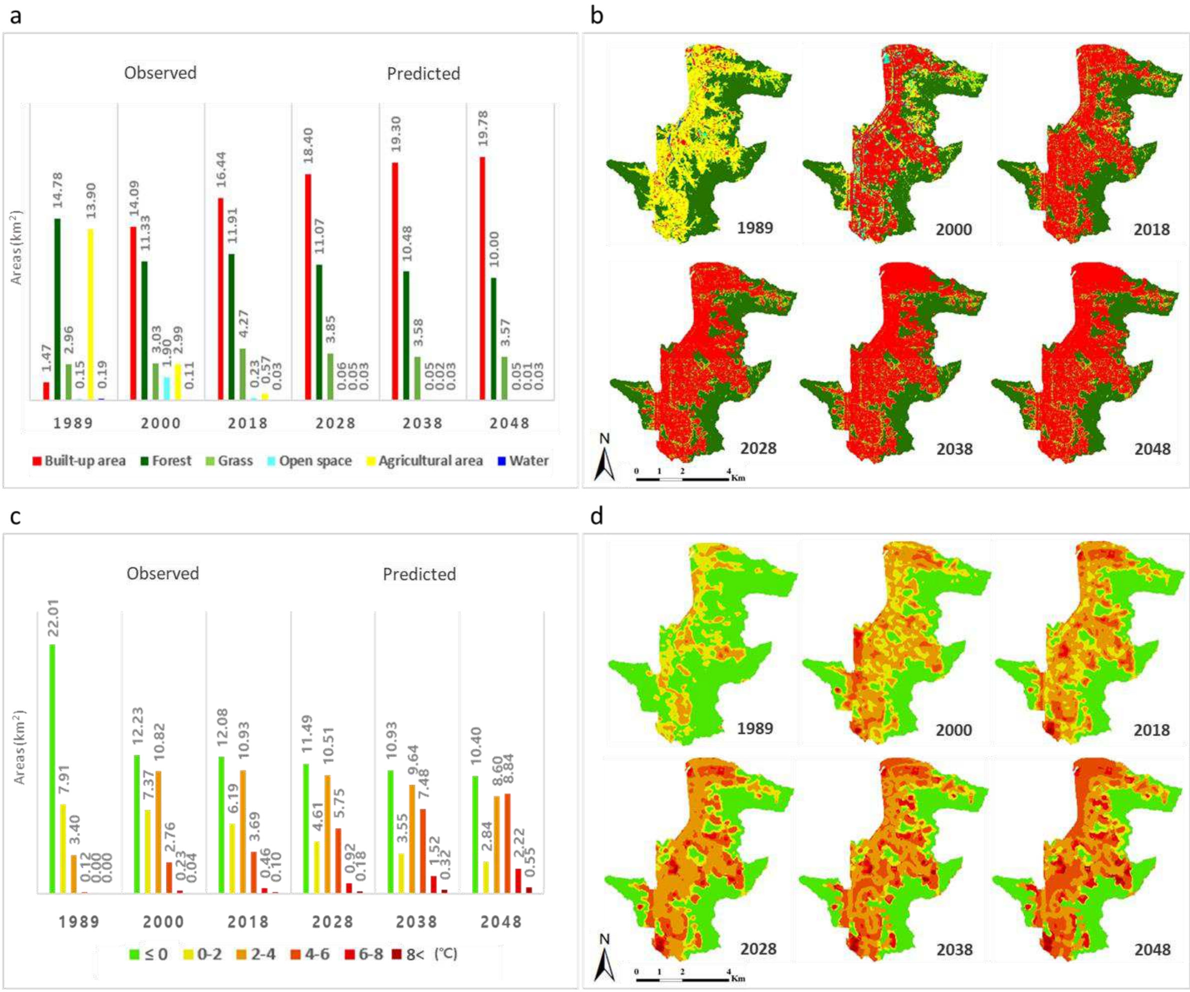

Fig. 2 SUHI distribution according to LULC changes from 1989 to 2048 in Bundang Newtown. a. Areas of LULC in Bundang Newtown from 1989 to 2048. **b**. LULC maps of Bundang Newtown from 1989 to 2048. **c.** Areas of SUHI distribution in Bundang Newtown from 1989 to 2048. **d**. SUHI distribution maps of Bundang Newtown from 1989 to 2048.

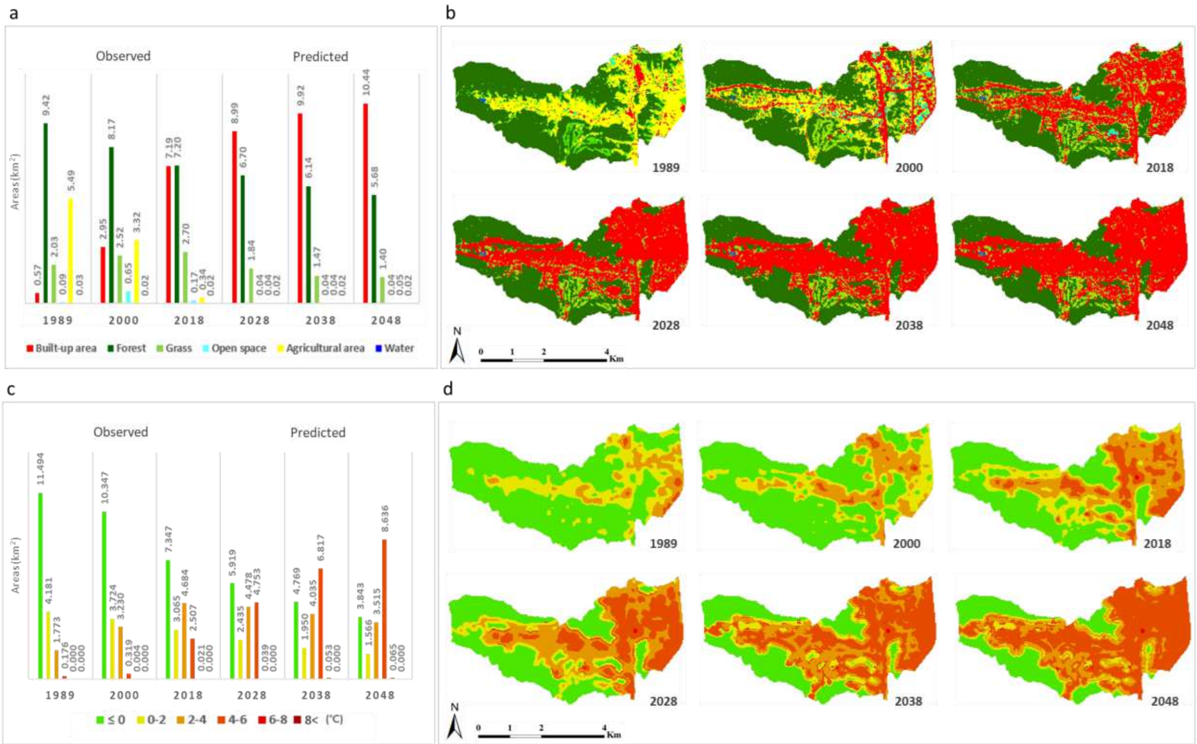

Fig. 3 SUHI distribution according to LULC changes from 1989 to 2048 in Pangyo Newtown. a. Areas of LULC in Pangyo Newtown from 1989 to 2048. **b.** LULC maps of Pangyo Newtown from 1989 to 2048. **c.** Areas of SUHI distribution in Pangyo Newtown from 1989 to 2048. **d.** SUHI distribution maps of Pangyo Newtown from 1989 to 2048.

Tables

Table 1. Development plan features for each Newtown

Division (unit)	**Bundang Newtown**	**Pangyo Newtown**
Generation of Newtown	1st generation	2nd generation
Development period	1989–1996	2003–2017
Whole area (km^2)	33.45	17.62
Development plan area (km^2)	19.64	8.9
Number of household (thousands)	97.6	29.3
Population density (number/ha)	199	98
Average greenspace ratio (%)	12–25	25–35
Transportation infrastructure	Vehicle-oriented	Public transportation-oriented

Acknowledgements

This work was conducted with the support of the Korea Environment Industry & Technology Institute (KEITI) through its Urban Ecological Health Promotion Technology Development Project, and funded by the Korea Ministry of Environment (MOE) (2020002770003).

Author contributions

K. Lee, S.H. Kim, and S.W. Jeon: research design; H.C. Sung and Y. Kim: data collection; K. Lee, Y. Kim, and H.C. Sung: empirical analysis; K. Lee and S.H. Kim: manuscript draft; and all authors: result interpretation and writing the paper.

Competing interests

The authors declare no competing interests.

Figures

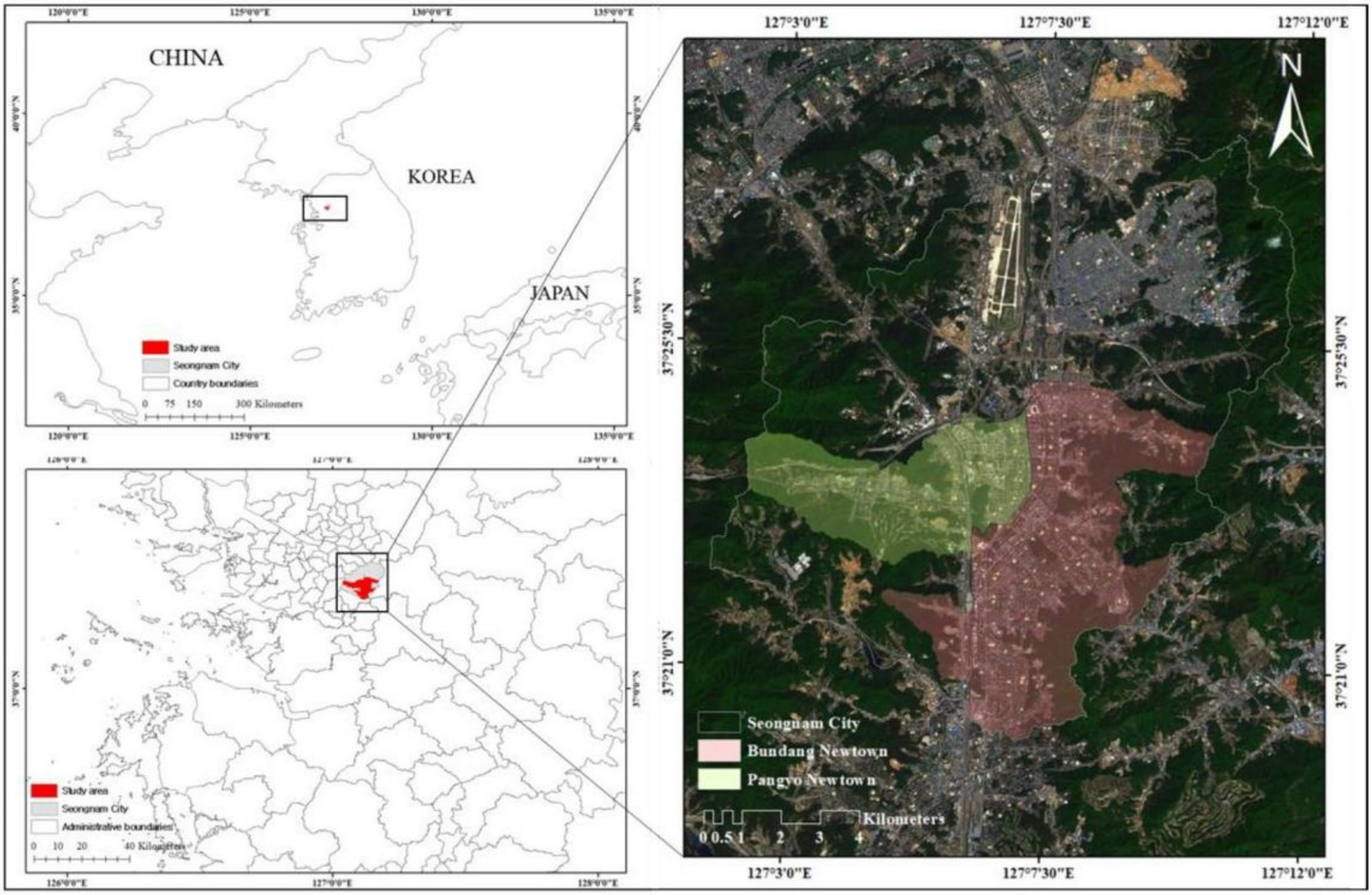

Figure 1

Map of study area. a. Geographical location of the two Newtowns. b. Enlarged image showing the Newtowns. c. Landsat OLI image acquired on May 09, 2018. Note: The designations employed and the presentation of the material on this map do not imply the expression of any opinion whatsoever on the part of Research Square concerning the legal status of any country, territory, city or area or of its authorities, or concerning the delimitation of its frontiers or boundaries. This map has been provided by the authors.

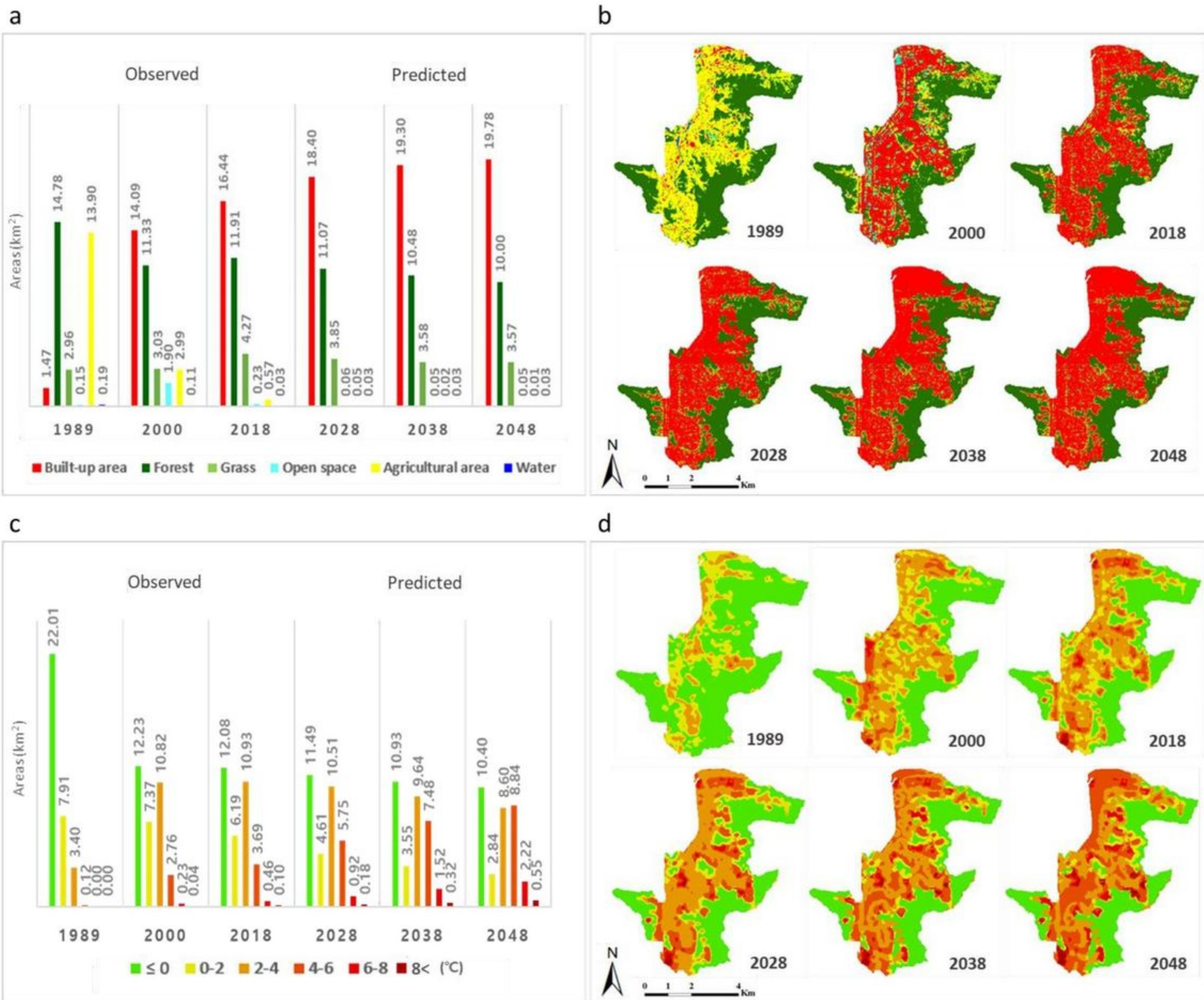

Figure 2

SUHI distribution according to LULC changes from 1989 to 2048 in Bundang Newtown. a. Areas of LULC in Bundang Newtown from 1989 to 2048. b. LULC maps of Bundang Newtown from 1989 to 2048. c. Areas of SUHI distribution in Bundang Newtown from 1989 to 2048. d. SUHI distribution maps of Bundang Newtown from 1989 to 2048. Note: The designations employed and the presentation of the material on this map do not imply the expression of any opinion whatsoever on the part of Research Square concerning the legal status of any country, territory, city or area or of its authorities, or concerning the delimitation of its frontiers or boundaries. This map has been provided by the authors.

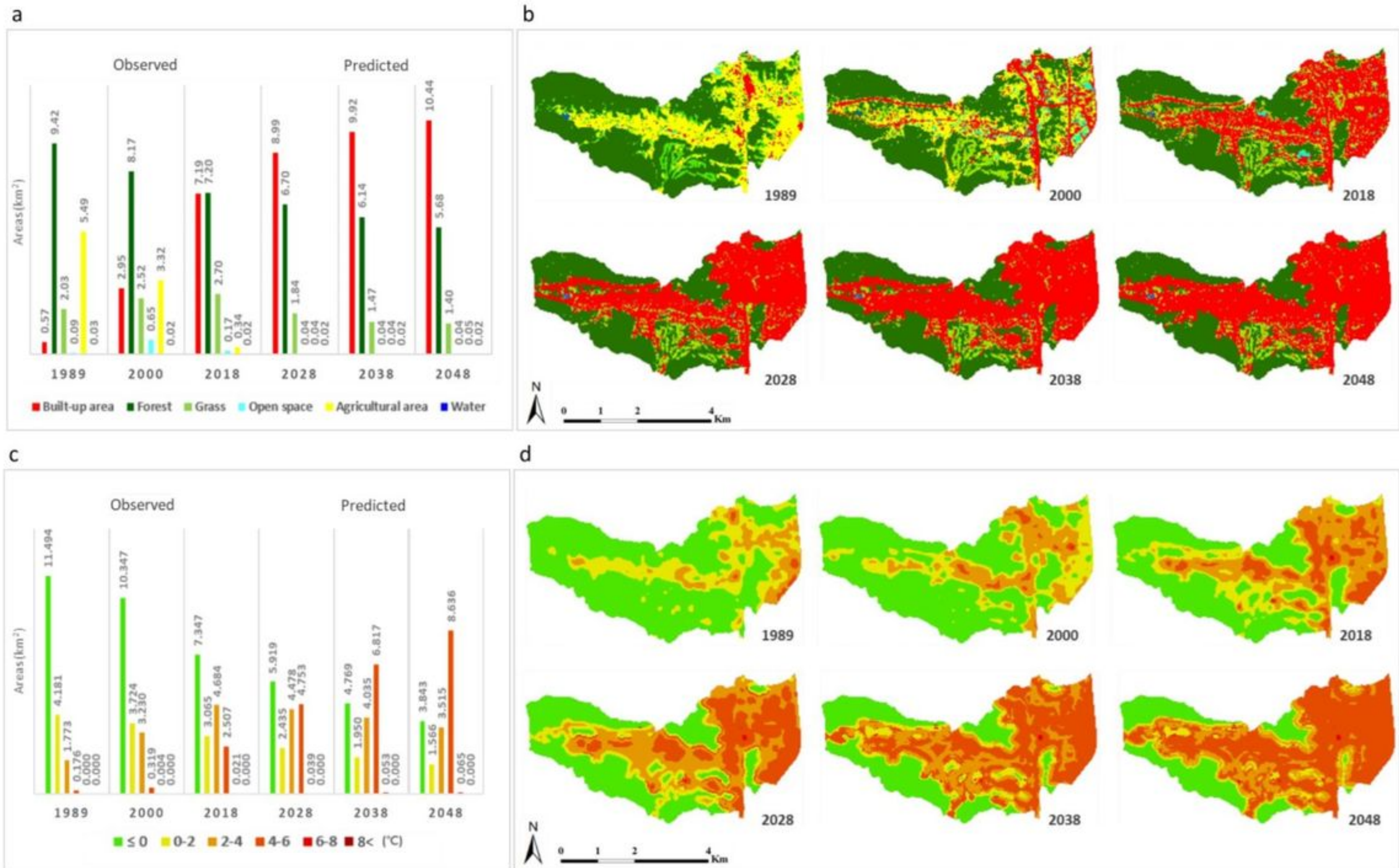

Figure 3

SUHI distribution according to LULC changes from 1989 to 2048 in Pangyo Newtown. a. Areas of LULC in Pangyo Newtown from 1989 to 2048. b. LULC maps of Pangyo Newtown from 1989 to 2048. c. Areas of SUHI distribution in Pangyo Newtown from 1989 to 2048. d. SUHI distribution maps of Pangyo Newtown from 1989 to 2048. Note: The designations employed and the presentation of the material on this map do not imply the expression of any opinion whatsoever on the part of Research Square concerning the legal status of any country, territory, city or area or of its authorities, or concerning the delimitation of its frontiers or boundaries. This map has been provided by the authors.